A&A 373, 786–795 (2001)
DOI: 10.1051/0004-6361:20010557

Astronomy & Astrophysics

An hydrodynamical model of the barred galaxy NGC 5850

J. A. L. Aguerri[1,2], J. H. Hunter[3], M. Prieto[1], A. M. Varela[1], S. T. Gottesman[3], and C. Muñoz-Tuñón[1]

[1] Instituto de Astrofisica de Canarias, 38200 La Laguna, Tenerife, Spain
[2] Astronomisches Institut der Universitat Basel, Venusstrasse 7, 4102 Binningen, Switzerland
[3] Department of Astronomy, University of Florida, Gainesville, FL 32611-2055, USA

Received 5 February 2001 / Accepted 28 March 2001

Abstract. We present the results of hydrodynamical model calculations of the barred galaxy NGC 5850 and compare to HI observations. The models assume a mass distribution for the galaxy which was obtained from photometrical I band observations. A pure bar perturbation model reproduces the HI observations in the inner 80″ of the galaxy. The reproduced morphological features are: the central gas concentration, the hole of gas in the bar region and the ring of HI located at the end of the bar. The spiral arms are not reproduced. The best model has the co-rotation located at 90″ and the mass of the bulge, bar, disk and halo are respectively: $4.7 \times 10^9\ M_\odot$, $4.6 \times 10^9\ M_\odot$, $4.9 \times 10^{10}\ M_\odot$ and $6.93 \times 10^{10}\ M_\odot$.

Key words. galaxies: individual: NGC 5850 – galaxies: kinematics and dynamics – galaxies: photometry – galaxies: structure

1. Introduction

The gas component of a spiral galaxy may play an important role in the formation and mantainence of the spiral structure (Lindblad 1996). The gas flow is also a response to gradients that appear in the underlying gravitational potential of the galaxy. These two reasons make studies of the gas in galaxies so important. The complexity of the above processes requires the use of numerical techniques. Hydrodynamical simulations are important tools to achieve an understanding of the gas behavior under the gravitational potential of the galaxy. Over the years, many important results have been obtained with such simulations.

The pioneering works were made during the 1970's (Sorensen et al. 1976; Sander & Huntley 1976). In their models, an axisymmetric disk is perturbed by a 2θ oval distortion or a bar-like perturbation. As a consequence of this perturbation spiral arms appeared in the disc of gas. Schwartz (1979, 1981) found a relation between the ring-like structures presented in some galaxies and the position of the resonances. That relation was observed in some real galaxies (Buta 1993). Another important observational event was obtained by Athanassoula (1992a,b). She explained the relation of the dust lanes that appear along the bars of some galaxies and the presence of inner Lindblad resonances (ILR).

Send offprint requests to: J. A. L. Aguerri,
e-mail: jalfonso@astro.unibas.ch

In recent years, realistic gravitational potentials have been obtained for models of some barred galaxies by using photometric images. Thus, the potentials used in the models of NGC 3992 (Hunter et al. 1988), NGC 1300 (England 1989), NGC 1073 (England et al. 1990) and NGC 3359 (Ball 1992) are formed by an axisymmetric part (disk and halo) and a perturbative part. The perturbation is composed of a triaxial bar and an oval distortion parallel to and corrotating with the bar. This oval distortion is added in order to reproduce the spiral structure of the galaxies. In the models of NGC 1365 (Lindblad et al. 1996) and NGC 1300 (Lindblad & Kristen 1996) the perturbation of the potential is taken as a Fourier series consisting of the cosine and sine 2θ, 4θ and 6θ-components.

Similar to the last models, a hydrodynamical model of NGC 5850 is presented in this paper. In Table 1 we summarize the most important parameters of this galaxy. This galaxy is of type $SB(r)ab$ (de Vaucouleurs et al. 1991, RC3) with a prominent bar, an inner ring and two spiral arms beginning before the end of the bar, forming an outer pseudo-ring. This galaxy has been studied by several other authors. Wozniak et al. (1995) have given the geometrical parameters for the nuclear and inner bar; Higdon et al. (1998) made a photometric and radio study of the galaxy; Prieto et al. (1997) determined the parameters of all structural components of the galaxy (bulge, disc, bar and ring). We will use these parameters in the gravitational potential of the galaxy.

The H_α image of this galaxy reveals star formation at the center, in the inner ring and in the arms, but not

Table 1. Parameters of NGC 5850.

Morphological type[a]	$SB(r)ab$
Observed $V_{\rm sys}^{b}$	2535
Distance[c]	33.8
Scale[d]	164
Photometric diameter (D_{25})[e]	21
Diameter of HI disk[f]	24.6
Mass within hydrogen disk[g]	2.09
Corrected blue luminosity[h]	11.47

[a] From de Vaucouleurs et al. 1991; RC3.
[b] Km s^{-1}, RC3
[c] Mpc. $H_0 = 75$ Mpc km s^{-1}.
[d] pc/arcsec.
[e] Kpc. RC3
[f] In Kpc. RC3
[g] In 10^9 solar masses.
[h] In magnitudes.

along the bar. There is a hole in the HI distribution in the bar region with a small amount of gas in the center, an HI inner ring and two HI spirals arms, one of them being broken, probably due to an interaction with NGC 5846 (Higdon et al. 1998). The model presented here will try to reproduce the HI structures within the inner ring region. The spiral arms will be very crudely reproduced and no attempts have been made to simulate the interaction.

The description of the observations and the decomposition of the surface brightness profile of NGC 5850 are presented in Prieto et al. (1997). Their study concludes that the surface brightness of the galaxy comes mainly from three structural components: an exponential disk, a $r^{1/4}$ bulge and a flat bar. The main parameters of these structures are presented in Table 2. Here we will assume a thin disk approximation. For the bulge + bar the spatial source distribution will be computed.

The aim of the present work is to determine the Corotation radius (CR) of the bar of NGC 5850 which explains the main morphological features within the inner ring region.

2. Spatial source distribution of the bulge and bar

Triaxial ellipsoids have been used to simulate bulges (Varela 1992; Varela et al. 1996) and bars (Hunter et al. 1988; Ball 1987, 1992) of spiral galaxies. We simulate the bulge + bar of NGC 5850 with such ellipsoids. The method used was developed and tested some years ago by: Varela (1992); Simonneau et al. (1993); Varela et al. (1996). A brief description of the method is given here.

The disc component obtained from the decomposition of the I luminosity profile was modeled using IRAF tasks, as a 2D flat disc, and subtracted from the image of the galaxy. Then, ellipses were fitted to the isophotes of the residuals. Those isocontours can be reproduced with a family of concentric ellipses that vary in position angle (PA) and ellipticity (ϵ) versus radius (semi-major axis

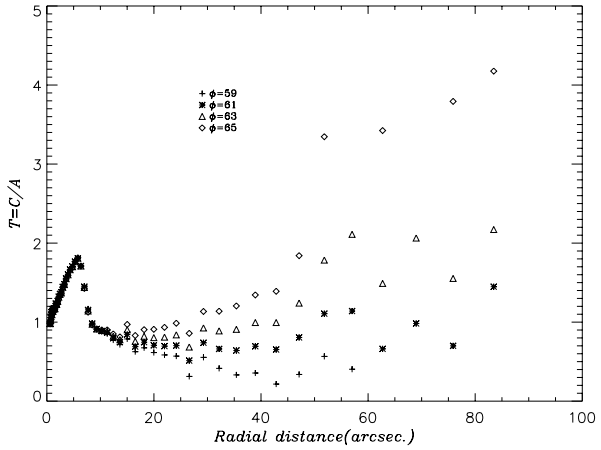

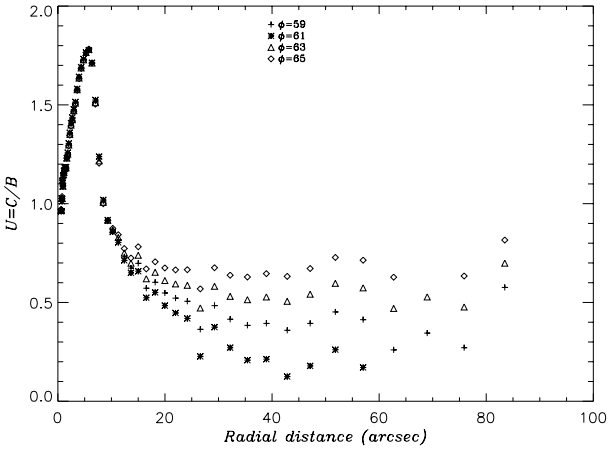

Fig. 1. Axial ratios (T, U) versus the ellipse's semi axis for each solution (ϕ; T, U) for the bulge and bar of NGC 5850.

length of the ellipses). We assume that these concentric ellipses are the projections on the plane of the sky of a family of concentric and coaxial ellipsoidal isoluminosity shells which form the structure of the bulge + bar of the galaxy. The solution is not unique, and several families of such ellipsoids reproduce the ellipses. Each family of possible solutions is parameterized by an angle, ϕ, which is the angle between the semi-major axis of the ellipsoid and the line of nodes of the galaxy.

In Fig. 1 we show the axial ratios, $T = C/A$ and $U = C/B$ (A, B and C being the semi-axis length of the ellipsoids; A is taken in the direction of the bar and C perpendicular to the galactic plane), for the different families of ellipsoids. In this figure it is important to note that for the inner $10''$, the axial ratios of all families of ellipsoids are $T = U$ and greater than 1. This means that they are prolate ellipsoids with $C > A = B$. Beyond the inner $10''$ the ellipsoids have $T \neq U$. These ellipsoids, then, correspond to a triaxial structure. Not all mathematical solutions of ellipsoids are physically possible. The solutions which are physically acceptable are those in which the

variation of T and U avoid possible intersections among the ellipsoids of the family. There are also some geometrical constrains (see Simonneau et al. 1998). Keeping this in mind, it is the family with $\phi = 59$ which best represents the structure bulge + bar of the galaxy.

Once the 3-D geometry of the bulge + bar is obtained, a spatial luminosity, $\rho_{\rm L}(\lambda)$, is assigned to each ellipsoid using the bulge + bar surface brightness profile. This surface brightness profile is the Abel transform of the spatial source distribution (Varela 1992; Varela et al. 1996). In Fig. 2 we show the spatial source distribution associated with the ellipsoids which build up the bulge + bar structure of NGC 5850.

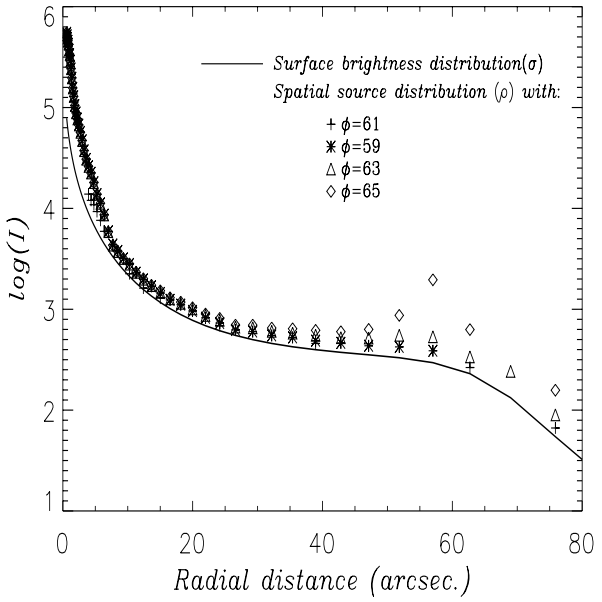

Fig. 2. Spatial source distribution, ρ, associated with the bulge and bar of NGC 5850 corresponding to different geometrical solutions (ϕ; T, U). The surface brightness distribution, σ, is also overplotted.

3. The gravitational potential and the velocity curve

Our aim with this hydrodynamical simulation is to simulate the behavior of the gas in the ring's region in the gravitational potential of NGC 5850. The modeled potential, ϕ, consists of the superposition of three components:

$$\Phi = \Phi_{\rm b} + \Phi_{\rm d} + \Phi_{\rm h}, \quad (1)$$

where $\Phi_{\rm b}$ is the bulge + bar potential, $\Phi_{\rm d}$ the disk potential and $\Phi_{\rm h}$ the halo. The only non-axisymmetric perturbation introduced into the gravitational potential is due to the bulge + bar. No other perturbations, such as oval distortion (Hunter et al. 1988) or spiral potential (Kaufmann & Contopoulos 1996), are considered here. The photometric information we have discussed earlier gives the distribution of the light in the galaxy. The mass-to-light ratio

Table 2. Photometric parameters in I band of NGC5850.

Bulge	$\Sigma_{\rm e}^a$ (mag/arcsec^2)	$r_{\rm e}(''$)	$L_\odot$	
	18.22 ± 0.15	7.7 ± 0.2	3×10^{10}	
Disk	$\Sigma_{\rm o}^c$ (mag/arcsec^2)	$r_{\rm o}^d(''$)	$L_\odot$	
	22.23 ± 0.1	43 ± 10	7.06×10^9	
Bar	$\Sigma_{\rm o}^e$ (mag/arcsec^2)	$r_{\rm o}^f(''$)	$r_1^g(''$)	$L_\odot$
	21.58	66.4	9.3	2.9×10^{10}

[a] Effective surface brightness of the bulge.
[b] Effective radius of the bulge.
[c] Central surface brightness of the disk.
[d] Scale length of the disk.
[e] Central surface brightness of the bar.
[f] Radial length scales along the major axis of the bar.
[g] Radial length scales along the minor axis of the bar.

allows us to determine the mass distribution. The HI velocity curve allows us to determine the mass-to-light for each component, and the dark matter distribution. In the following subsections we summarize the potential and the velocity curve of each component.

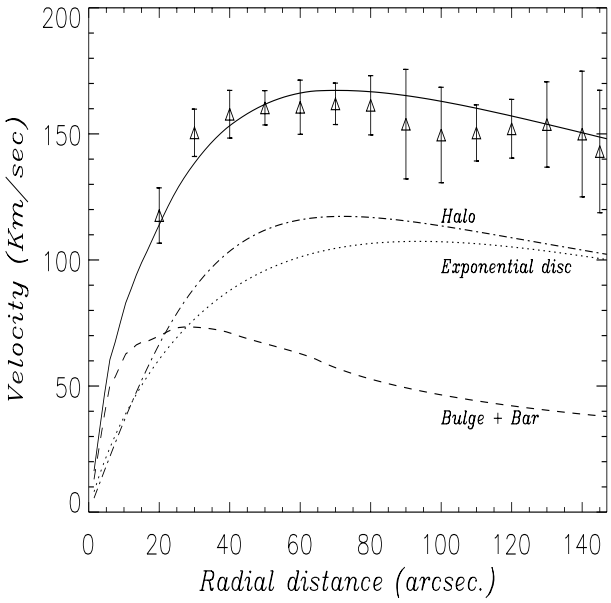

Fig. 3. The observed velocity curve (triangles) fitted with the curves corresponding to the disk (dotted line), halo (dotted-dashed line) and bulge and bar (dashed line).

3.1. The axisymmetric disk

The surface brightness profile of NGC 5850 fits well with the exponential disk (Prieto et al. 1997) whose parameters are given in Table 2. The absence of prominent color gradients in the disc allows us to assume a constant mass-to-light ratio, $(M/L)_{\rm D}$. Such a disk of surface brightness, $\Sigma(r) = \Sigma_{\rm o} {\rm e}^{-r/r_{\rm d}}$ ($\Sigma_{\rm o}$ being the surface brightness at the

origin and $r_{\rm d}$ the scale length of the disc), produces a gravitational potential given by (Freeman 1970):

$$\Phi(r) = -\pi G\Sigma_{\rm o} r(M/L)_{\rm D}[I_0(y)K_1(y) - I_1(y)K_0(y)], \quad (2)$$

where I_n and K_n are the modified Bessel functions of the first and second kinds, evaluated at $y = \frac{r}{2r_{\rm d}}$ and $(M/L)_{\rm D}$ is the mass-to-light ratio for the disc. The total mass of the disk is:

$$M = 2\pi\Sigma_{\rm o}(M/L)_{\rm D} r_{\rm d}^2. \quad (3)$$

A particle orbiting in this potential has a circular velocity:

$$v_{\rm d}^2(r) = 4\pi G\Sigma_{\rm o}(M/L)_{\rm D} r_{\rm d} y^2[I_{\rm o}(y)K_0(y) - I_1(y)K_1(y)]. \quad (4)$$

This rotation curve has a sharp initial rise and reaches a maximum velocity at $r \sim 2r_{\rm d}$. After this maximum the velocity quickly approaches Keplerian.

3.2. The bulge and bar structure

As explained in Sect. 2, the spatial light distribution of the bulge + bar structure is distributed in isoluminosity shells. Taking a mass-to-light ratio, we derive the spatial mass density, ρ. If we simulate the bulge + bar structure with N isomass shells, the gravitational potential due to this structure at a point (x, y, z), in a reference frame centered on the galactic center, where x is the mayor axis of the ellipsoids and z the perpendicular direction to galactic plane, will be:

$$\Phi_{\rm b}(x,y,z) = \Phi_{A_1B_1C_1\rho_1}(x,y,z)$$

$$+ \sum_{i=2}^{N}[\Phi_{A_iB_iC_i\rho_i}(x,y,z) - \Phi_{A_{i-1}B_{i-1}C_{i-1}\rho_i}(x,y,z)], \quad (5)$$

$\Phi_{a_ib_ic_i\rho_j}(x,y,z)$ being the potential created by homogeneous solid ellipsoid of semi-axis length a_i, b_i, c_i and density ρ_j at the point (x, y, z). Two such ellipsoids (triaxial and prolate) are presented in our bulge + bar structure.

For a triaxial ellipsoid with semi-axis length $A > B > C$ and constant density, ρ, the gravitational potential in a point of coordinates $(x, y, 0)$ is (MacMillian 1958):

$$\Phi_{\rm b}(x,y,0) = -\frac{2\pi G\rho ABC}{\sqrt{A^2-C^2}}\Bigg(\left[1 - \frac{x^2}{A^2-B^2} + \frac{y^2}{A^2-B^2}\right]$$

$$F(w_k,k) + \left[\frac{x^2}{A^2-B^2} - \frac{(A^2-C^2)y^2}{(A^2-B^2)(B^2-C^2)}\right]E(w_k,k)$$

$$+ \left[\frac{C^2+k}{B^2-C^2}y^2\right]\frac{\sqrt{A^2-C^2}}{\sqrt{A^2+k}\sqrt{B^2+k}\sqrt{C^2+k}}\Bigg), \quad (6)$$

where $F(w_k, k)$, $E(w_k, k)$ are the first and second elliptical integrals, respectively, $w_k = \sqrt{\frac{A^2-C^2}{A^2+k}}$ and $k = 0$ if the point is inside of the ellipsoid, or k is the largest root of

$$\frac{x^2}{A^2+k} + \frac{y^2}{B^2+k} = 1 \quad (7)$$

if the point is outside of the ellipsoid.

For a prolate ellipsoid of semi-axis length $C > A = B$, the gravitational potential at a point $(x, y, 0)$ is (MacMillian 1958):

$$\Phi_{\rm b}(x,y,0) = \pi G\rho A^2 C(1 + \frac{x^2+y^2}{2(C^2-A^2)})\frac{2}{\sqrt{C^2-A^2}}$$

$$\sin{\rm h}^{-1}(\sqrt{\frac{C^2-A^2}{A^2+k}}) - \pi G\rho A^2 C\frac{\sqrt{C^2+k}}{C^2-A^2}\frac{x^2+y^2}{A^2+k} \quad (8)$$

where $k = 0$ for internal points, and for external points is the largest root of the equation

$$\frac{x^2+y^2}{A^2+k} = 1. \quad (9)$$

We can estimate the angle-averaged rotation speed, $v_{\rm b}$, due to the bulge + bar structure as (Kaufmann & Contopoulos 1996):

$$v_{\rm b}^2(r) = \frac{2}{\pi}\int_0^{\pi/2} r\frac{{\rm d}\Phi_{\rm b}(r,\theta)}{{\rm d}r}{\rm d}\theta \quad (10)$$

$\Phi_{\rm b}(r, \theta)$ being the corresponding potential of the triaxial or prolate ellipsoid in cylindrical coordinates.

3.3. The halo component

A spherical halo of dark matter is needed in order to fit the flat part of the HI velocity curve at large radii (Rubin et al. 1978; Bosma 1981). The halo of dark matter was simulated assuming that the matter is distributed in a Plummer sphere of density (Kaufmann & Contopoulos 1996):

$$\rho_{\rm h}(r) = \frac{3M_{\rm h}}{4\pi b_{\rm h}^3}\left(1 + \frac{r^2}{b_{\rm h}^2}\right)^{-5/2} \quad (11)$$

$M_{\rm h}$ being the total mass of the halo and $b_{\rm h}$ is a shape parameter. The gravitational potential produced by this mass distribution is:

$$\Phi_h(r) = -\frac{GM_h}{\sqrt{r^2+b_h^2}}. \quad (12)$$

Assuming gravitational equilibrium, the velocity curve of such a halo is given by:

$$v_{\rm h}(r) = r\sqrt{\frac{GM_{\rm h}}{(r^2+b_{\rm h}^2)^{3/2}}}. \quad (13)$$

3.4. The HI velocity curve and the mass-to-light ratio

The angle-averaged HI rotation curve was obtained for this galaxy from HI observations of NGC 5850 kindly provided by R. Buta. The rotation curve was fitted assuming an inclination of 25° and the line of nodes at 330°. The rotation curve obtained is similar to the velocity curve given by Higdon et al. (1998) in the undisturbed side of the galaxy.

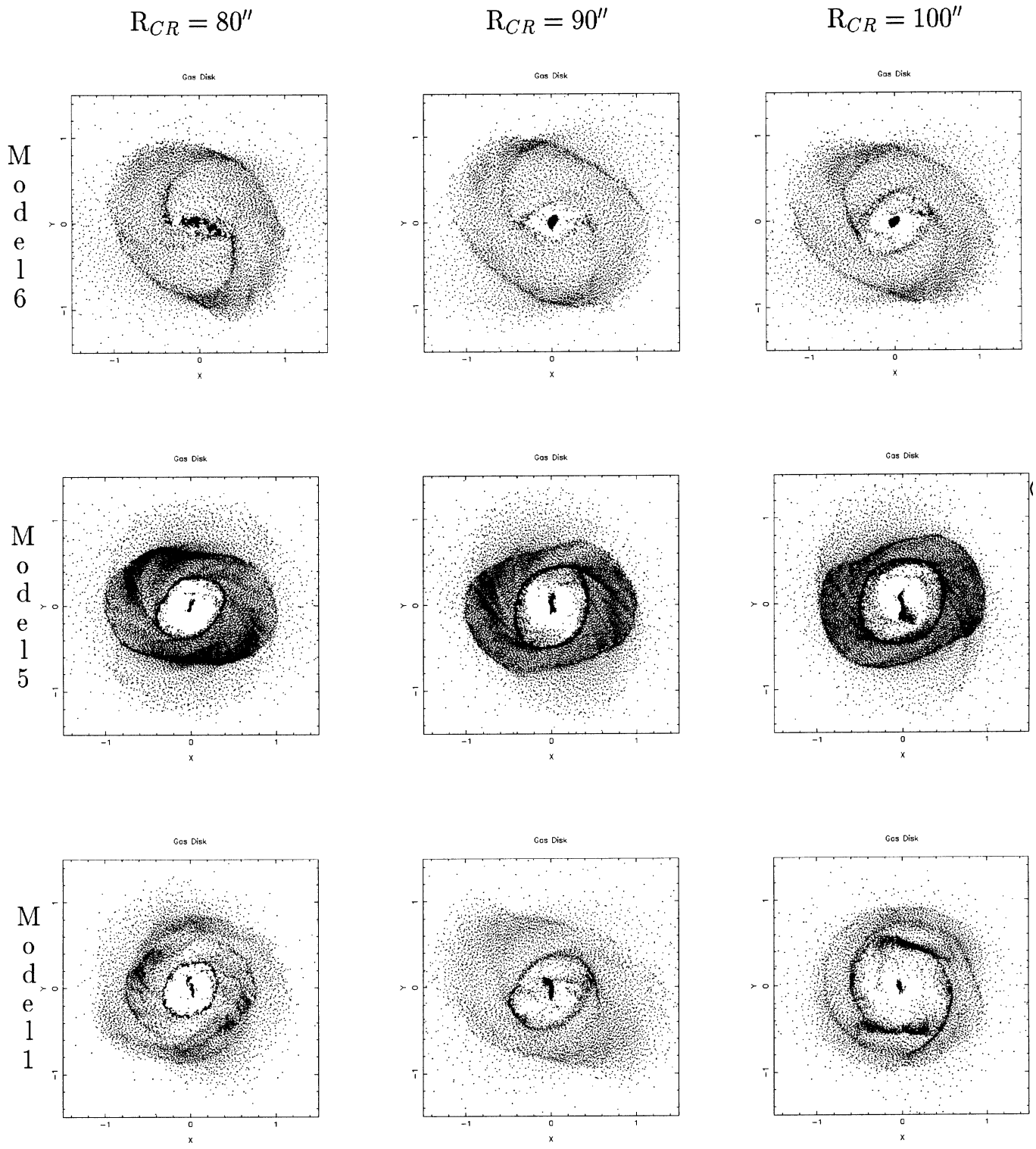

Fig. 4. Particle distribution of models 1, 5 and 6 (see Table 3). For each we show three models with CR located at: 80″, 90″ and 100″. The x and y axis are in arbitrary units (see text for details).

At a fixed galactocentric distance, the total rotation velocity, $v_{\rm t}(r)$, generated by disk, halo, bulge + bar is obtained from their individual contribution according to:

$$v_{\rm t}^2(r) = v_{\rm d}^2(r) + v_{\rm h}^2(r) + v_{\rm b}^2(r). \quad (14)$$

For the best model, which will be described in the next section, the observational HI velocity curve was fitted using a mass-to-light ratio (in I band) for the disk of 7 and 0.15 for the bulge + bar structure. This low mass-to-light ratio of the bulge + bar structure is due to the strong luminosity in the I band of the galaxy in that region. Models

Table 3. Hydrodynamical models of NGC 5850.

	$M^a_{\rm bulge}$	$M^b_{\rm bar}$	$M^c_{\rm disk}$	$M^d_{\rm halo}$	$b^e_{\rm h}$	$(M_{B+B}/M_d)^f$	$M^g_{\rm T}$
Model 1	6.3×10^9	6.09×10^9	4.24×10^{10}	8.06×10^{10}	9.84	0.29	1.35×10^{11}
Model 2	5.1×10^9	4.93×10^9	4.95×10^{10}	8.42×10^{10}	11.56	0.20	1.43×10^{11}
Model 3	6.9×10^9	6.67×10^9	5.66×10^{10}	5.66×10^{10}	9.84	0.23	1.26×10^{11}
Model 4	4.5×10^9	4.3×10^9	4.24×10^{10}	6.78×10^{10}	7.38	0.20	1.19×10^{11}
Model 5	4.7×10^9	4.6×10^9	4.95×10^{10}	6.93×10^{10}	8.61	0.18	1.28×10^{11}
Model 6	2.87×10^9	2.78×10^9	5.66×10^{10}	5.09×10^{10}	7.38	0.09	1.13×10^{11}

[a] Mass of the bulge in solar masses.
[b] Mass of the bar in solar masses.
[c] Mass of the disk in solar masses.
[d] Mass of the halo in solar masses.
[e] Shape parameter of the halo, in Kpc.
[f] Mass of the bulge + bar over mass of the disc.
[g] Total mass of the galaxy.

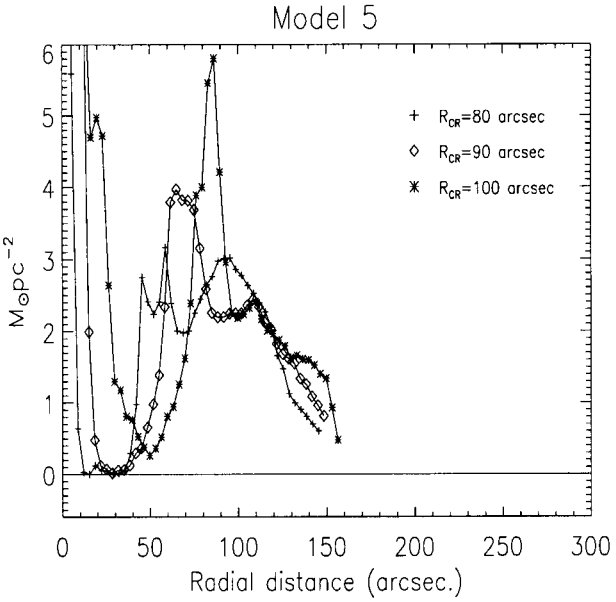

Fig. 5. The angle average surface mass densities of HI versus radial distance for three models with the same mass distribution as model 5 (see Table 3). The three models have different CR located at: 80″ (crosses), 90″ (diamonds) and 100″ (asterisks).

with higher mass-to-light ratios in the bulge + bar region cannot reproduce the HI features of the galaxy. We can obtain, from the values in the I band, the total mass-to-light ratio of the galaxy in B band. This value is 2.83. Rubin et al. (1982) studied 23 *Sb* galaxies such as NGC 5850. They obtained values for the mass-to-light ratio in B between 2.04 and 15.4 (see Fig. 5a, Rubin et al. 1982) with a median value of 4.4 ± 0.4. Although our value is less than the median, it is in the interval of values obtained by these authors. In Fig. 3 we show the fit of the velocity curve for the best model.

4. The hydrodynamical model

Before presenting the hydrodynamical model, we give a brief description of the code.

4.1. The numerical code

The code used in this study was developed by Heller & Shlosman (1994). The hydrodynamic of the gas is treated using the smoothed particle hydrodynamic method (SPH method) introduced by Lucy (1977) and Gingold & Monaghan (1977).

The SPH method represents the fluid elements constituting a system of particles which evolves according to the dynamical equations obtained from the hydrodynamic conservation laws in their Lagrangian form. This formalism uses a finite number of particles, N, to approximate the continuum limit. The particles in the fluid elements are smoothed out to a radius ($2h$) by a particular kernel. The length h is known as the smoothing length, which must be chosen so that there are enough neighbors within the ($4h^3$) box. A common choice is 32 particles. The kernel employed in the code is that proposed by Monaghan & Lattanzio (1985).

The particles evolve into the phase space, obeying the equations of motion. The gravitational potential, Φ_i, is an external potential computed as explained in the previous section. In all our models the interstellar medium is considered as an isothermal gas with a sound speed of 15 km s^{-1} for the best model. Some models with an adiabatic inter-stellar medium were run with no satisfactory results.

4.2. The models

Several models were run in order to reproduce the structural features observed in the HI data of NGC 5850. All models begin with the particles initially randomly distributed in a circular disc of radius 24.6 Kpc and

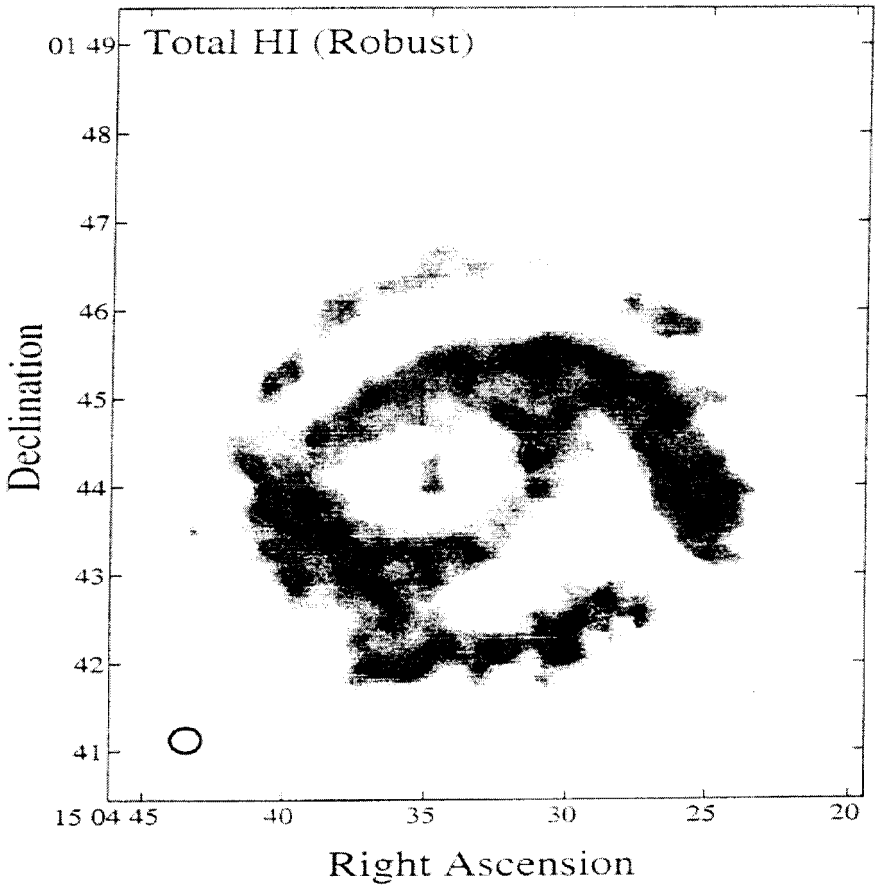

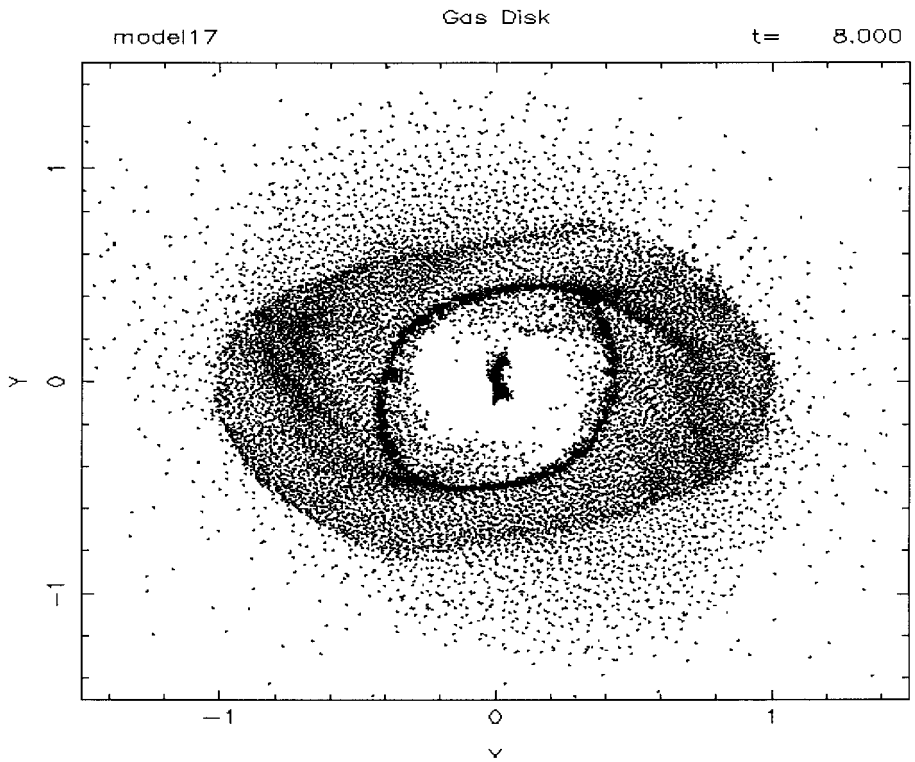

Fig. 6. (Top) HI distribution of NGC 5850, taken from Higdon et al. (1998). (Bottom) particle distribution of the best model. The x and y axis are in arbitrary units (see text for details).

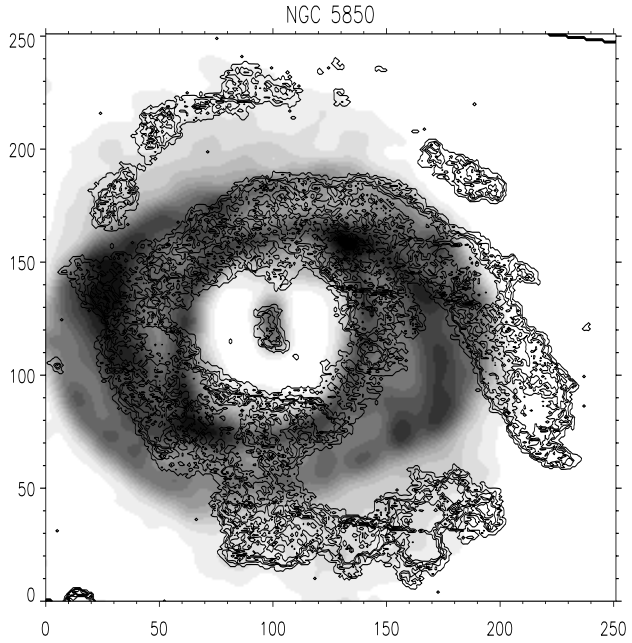

Fig. 7. Observational HI distribution (contours) of NGC 5850. Overplotted is the particles distribution of the best model (shadows). The particle distribution has been smoothed to the same spatial resolution as the observations using a Gaussian filter. The x and y axis are in arbitrary units (see text for details).

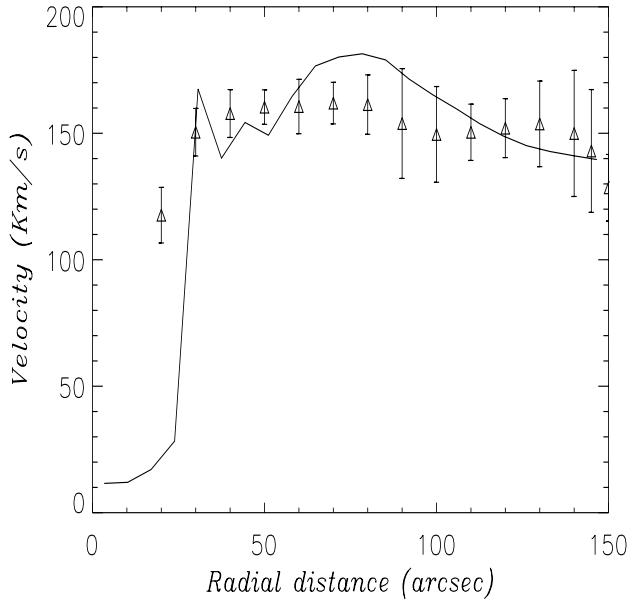

Fig. 8. Observed rotation curve (triangles) and rotation curve obtained from the best model (full line).

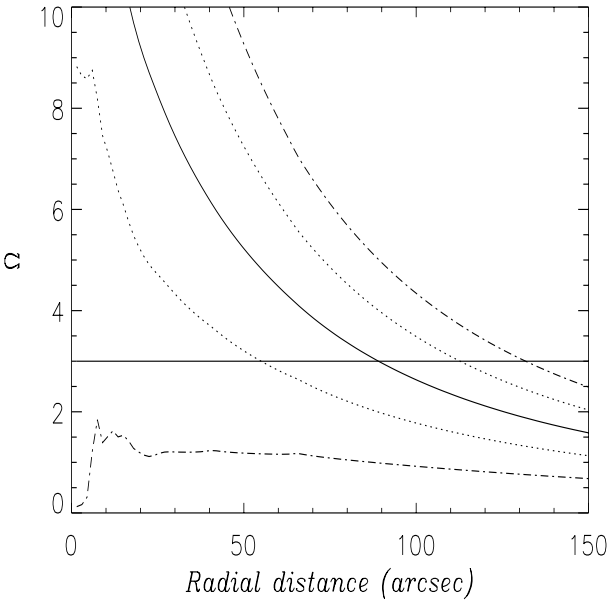

Fig. 9. Diagram of frequencies associated with the velocity curve of Fig. 3. The angular rotation, Ω, is the solid line, the dotted lines correspond to $\Omega \pm \kappa/4$, the dashed-dotted lines represent $\Omega \pm \kappa/2$ and the horizontal solid line is the pattern speed. The x-axis is in arcsec. and the y-axis is in arbitrary units.

$2.09 \times 10^9\ M_\odot$ (Huchtmeier & Richter 1989). These particles evolve under the gravitational potential explained in Sect. 3. The axisymmetric parts of this potential (disk and halo) are swichted on from the beginning of the simulations. The non-axisymmetric part (bar and bulge) is introduce gradually according to (Laine et al. 1998):

$$\frac{(\text{Bulge} + \text{Bar})\text{force}(t)}{\text{Final}(\text{Bulge} + \text{Bar})\text{force}} = (3 - \frac{2t}{t_\text{b}})(\frac{t}{t_\text{b}})^2 \qquad (15)$$

where t_b is the time at which the potential of the bulge + bar is totally introduced. In our simulations, that time is about 1 revolution of the bar.

The free parameters which are varied from one model to another one are: mass of the disk, mass of the bulge and bar, pattern speed, mass of the halo and the shape parameter of the halo, b_h. The parameters of the models are shown in Table 3.

Three different models with different pattern speeds were run for a fixed mass of the disk, halo and bulge + bar. The locations of CR in these models are at: 80″, 90″ and 100″. Figure 4 shows models with three different mass distributions. They have the same mass distributions as models 1, 5 and 6 from Table 3. We also show three different models with different CR for each mass distribution. The mass of the bulge + bar structure is increased from model 6 to model 1. The bulge + bar structure of model 6 is 9% that of the disc. The ring structure is not well defined in this model. For model 1 the mass of the bulge + bar is 28% of the mass of the disc. The ring is defined but it is perturbed due to the force of the prominent bulge + bar structure. As we will see bellow, model 5 is the one with the best parameters of all the structures presented in the HI distribution.

It is observed that the position of the HI ring is controlled by the position of the CR. Figure 5 shows the angle average surface mass density of HI for our model 5 for three values of CR: 80″, 90″ and 100″. The radius of the ring is at 76″, which is in a very good agreement with the position given by Higdon et al. (1998) (Fig. 13) and

the measurement, in $B-I$ color map made by Prieto et al. (1997). Only those models with CR at 90″ produce an HI ring at this radial distance. This model also reproduces the observed mass surface density of the ring. The shape of the ring of model 5 is also in agreement with the observed one. The axial ratio between its semi-minor and semi-major axis lengths is about 0.77″. Similar intrinsic values were obtained by Prieto et al. (1997), namely 0.82 ± 0.04.

One more structural feature can help us to decide which is the best model. It is the existence of a HI hole in the ring region with a small accumulation of gas in the center. These features are controlled by varying the mass of the components in the gravitational potential. The best model which reproduces all of these structures is Model 5 (Fig. 6). For this model, the mass of the bulge and bar is 18% of that of the disc. Models with less mass in the perturbed potential cannot create the absence of gas in the bar region and models with more massive bars and bulges disturb the disk too much.

Figure 7 shows the observed HI distribution (contours) and the particle distribution of model 5 (shadows). The particle distribution of the model has been smoothed by a Gaussian filter in order to have the same spatial resolution in the observations and in the model. It can be appreciated from Fig. 6 the good agreement of the observations and model in the inner 80″ of the galaxy. Figure 8 shows the velocity curve of the galaxy and the rotation curve obtained from model 5. It can be noted from Fig. 7 that the shape of the HI spiral arms are not well reproduce by the model. The spiral arms of barred galaxies in hydrodynamical models have been reproduced, including oval distortions (Hunter et al. 1988) or spiral potentials (Kaufmann & Contopoulos 1996) to the gravitational potential of the galaxies. We have not tried these potentials in our model because even with the inclusion of this potential it is hard to explain the distorted arms of this galaxy. This distortion is due to the interaction of NGC 5850 with NGC 5846 (Higdon et al. 1998).

The contribution to the total force of the galaxy due to the perturbed part of the potential is 26%, which indicates that the perturbation is quite strong. Similar values have been found in other simulations, notably for NGC 3992 (Kaufmann & Contopoulos 1996). Figure 9 shows the position of the main resonances of NGC 5850 using the linear approximation. CR is located at 90″, beyond the end of the bar. The position of the ring, about 76″, is between the I4:1 resonance and CR. Although this galaxy has a secondary bar (Prieto et al. 1997; Wozniak et al. 1995) there is no ILR presented in Fig. 9. This is because the linear approximation is a rough approximation due to the strong bar of this galaxy. The fit of the velocity curve in the inner region is poor due to the absence of HI in that region. Futher, we have no information about the inner 20″ and we cannot say anything about its kinematical features here.

The location of CR at 90″ implies that the pattern speed of the bar, $\Omega_{\rm b}$ is 10.3 km s^{-1} kpc^{-1}. This is quite slow (see Aguerri et al. 1998, Table 3), that could be explained due to the interaction of NGC 5850 with NGC 5846. Miwas & Noguchi (1998) showed that tidally induced bars rotate quite slowly.

In order to determine how the bulge structure affects the results of the model, we have run models without the bulge. Taking the axial ratios T and U of the most external ellipsoids, a triaxial bar was created. Two models were run. One without the mass of the bulge and with the mass of the bar distributed among the ellipsoids and another one with the mass of the bulge and bar in the new triaxial bar. It is observed that in both, the ring structure appears, but the gas is not present in the correct amount in the center. This implies that the prolate inner structure plays an important role in the formation of this central structure.

5. Conclusions

The behavior of the HI gas in the gravitational potential of NGC 5850 is presented. The gravitational potential has been derived from near-infrared observations in I band. This potential is build up by an axisymmetric exponential disk, an spherical halo of dark matter and an ellipsoidal bulge and bar structure. Using the HI velocity curve, the mass-to-light ratio of the disk, bulge and bar were fitted.

The best model which reproduces all structural features of the HI distribution has the following characteristics:

1. CR is located at 90″, beyond the end of the bar.
2. The position of the HI ring is located between the I4:1 resonance and CR.
3. No ILR appear in the model.
4. The mass of the bulge, bar, disk and halo are respectively: 4.7×10^9 $M_\odot$, 4.6×10^9 $M_\odot$, 4.9×10^{10} $M_\odot$, 6.93×10^{10} $M_\odot$.
5. The mass of the perturbative part (bulge and bar) is 18% of the mass of the disk and contributes 26% of the total force of the galaxy.

We emphasize that the bar + bulge structures as we have modeled them, with their strong forcing terms, can stir the disk and reproduce the HI features in the inner 80″ of the galaxy. However, other components, such as oval distortions or a spiral potential obtained from photometric observations or interactions with NGC 5846, will be necessary to model rigorously the spiral structures of the disk.

Acknowledgements. JALA was partially soported by grant 20-56888.99 from the Schewizerischer Nationalfonds. The 2.5-m INT is operated on the island of La Palma by the Royal Greenwich Observatory at the Spanish *Observatorio del Roque de Los Muchachos* of the *Instituto de Astrofísica de Canarias*. Support for this work comes from project PB97-1107 of the Spanish DGES. The observations received financial support from the European Commission through the Access to Large-Scale Facilities Activity of the Human Capital and Mobility Programme.

References

Aguerri, J. A. L., Beckman, J. E., & Prieto, M. 1998, AJ, 116, 2136

Athanassoula, E. 1992a, MNRAS, 259, 328

Athanassoula, E. 1992b, MNRAS, 259, 345

Ball, R. 1987, ApJ, 307, 453

Ball, R. 1992, ApJ, 395, 418

Boroson, T. 1981, ApJS, 46, 177

Bosma, A. 1981, AJ, 86, 1791

Buta, R. 1993, PASP, 105, 654

de Vaucouleurs, G., de Vaucouleurs, A., Corwin, H. G., et al. 1991, Third Reference Catalogue of Bright Galaxies (Springer, New York), (RC3)

England, M. N. 1989, ApJ, 344, 669

England, M. N., Gottesman, S. T., & Hunter, J. H. 1990, ApJ, 348, 456

Freeman, K. C. 1970, ApJ, 160, 811

Gingold, R. A., & Monaghan, J. J. 1977, MNRAS, 181, 375

Heller, C. H., & Shlosman, I. 1994, ApJ, 424, 84

Higdon, J. L., Buta, R. J., & Purcell, G. B. 1998, AJ, 115, 80

Huchtmeier, W. K., & Richter, O. G. 1989, A General Catalog of HI Observations of Galaxies (Springer-Verlag, New York)

Hunter, J. H., Ball, R., Huntley, J. M., England, M. N., & Gottesman, S. T. 1988, ApJ, 324, 721

Kaufmann, D. E., & Contopoulos, G. 1996, A&A, 309, 381

Laine, S. J., Shlosman, I., & Heller, C. 1998, MNRAS, 297, 1052

Lindblad, P. A. B. 1996, Ph.D. Thesis, Stockholm University

Lindblad, P. A. B., Lindblad, P. O., & Athanassoula, E. 1996, A&A, 313, 65

Lindblad, P. A. B., & Kristen, H. 1996, A&A, 313, 733

Lucy, L. 1977, ApJ, 82, 1013

MacMillian, W. D. 1958, Theoretical Mechanics: The Theory of the Potential, New York: Academic

Miwa, T., & Noguchi, M. 1998, ApJ, 499, 149

Monaghan, J. J., & Lattanzio, J. C. 1985, A&A, 149, 135

Prieto, M., Gottesman, S. T., Aguerri, J. A. L., & Varela, A. M. 1997, AJ, 114, 1413

Rubin, V. C., Thonnard, N., & Ford, W. K. Jr. 1978, ApJ, 225, 107

Rubin, V. C., Ford, W. K., & Thonnard, N. 1982, ApJ, 261, 439

Sanders, R. M., & Huntley, J. M. 1976, ApJ, 209, 53

Schwartz, M. P. 1979, Ph.D. dissertation, Australian National Observatory

Schwartz, M. P. 1981, ApJ, 247, 77

Simonneau, E., Varela, A. M., & Muñoz-Tuñón, C. 1993, J. Quant, Spectrosc. & Rad. Transf., 49, 149

Simonneau, E., Varela, A. M., & Muñoz-Tuñón, C. 1998, Il Nuovo Cimento, 113, 927

Sorensen, S. A., Matsuda, T., & Fujimoto, M. 1976, ApJSS, 43, 491

Stark, A. A. 1977, ApJ, 213, 368

Varela, A. M. 1992, Ph.D. dissertation, Universidad de La Laguna

Varela, A. M., Muñoz-Tuñón, C., & Simmoneau, E. 1996, A&A, 306, 381

Wozniak, H., Friedli, D., Martinet, L., & Bratschi, P. 1995, A&AS, 111, 115